Journal of Magnetic Resonance 228 (2013) 104–115

Contents lists available at SciVerse ScienceDirect

Journal of Magnetic Resonance

journal homepage: www.elsevier.com/locate/jmr

Estimation of petrophysical and fluid properties using integral transforms in nuclear magnetic resonance

Fred K. Gruber, Lalitha Venkataramanan *, Tarek M. Habashy, Denise E. Freed

Schlumberger-Doll Research, One Hampshire Street, Cambridge, MA 02139, United States

ARTICLE INFO

Article history:
Received 14 September 2012
Revised 15 December 2012
Available online 9 January 2013

Keywords:
Integral transform
Analysis of exponentially decaying data
Analysis of NMR data in inhomogeneous fields
Inverse Laplace transform
NMR logging

ABSTRACT

In the past decade, low-field NMR relaxation and diffusion measurements in grossly inhomogeneous fields have been used to characterize properties of porous media, e.g., porosity and permeability. Pulse sequences such as CPMG, inversion and saturation recovery as well as diffusion editing have been used to estimate distribution functions of relaxation times and diffusion. Linear functionals of these distribution functions have been used to predict petro-physical and fluid properties like permeability, viscosity, fluid typing, etc. This paper describes an analysis method using integral transforms to directly compute linear functionals of the distributions of relaxation times and diffusion without first computing the distributions from the measured magnetization data. Different linear functionals of the distribution function can be obtained by choosing appropriate kernels in the integral transforms. There are two significant advantages of this approach over the traditional algorithm involving inversion of the distribution function from the measured data. First, it is a direct linear transform of the data. Thus, in contrast to the traditional analysis which involves inversion of an ill-conditioned, non-linear problem, the estimates from this new method are more accurate. Second, the uncertainty in the linear functional can be obtained in a straight-forward manner as a function of the signal-to-noise ratio (SNR) in the measured data. We demonstrate the performance of this method on simulated data.

1. Introduction

Our study has been guided by NMR applications in porous media such as rocks and well-logging. For example, NMR can provide certain properties of rocks like porosity, movable fluid porosity, permeability, and pore size distribution [1]. These applications use "inside-out" NMR apparatus for *in situ* evaluation of geological formations in boreholes at depths up to 10 km and temperatures up to 200 °C [1–3]. In these applications, the measured NMR magnetization data denoted by $G(t)$ is a multi-exponential decay, with a continuum of relaxation times T_2 [2,3],

$$G(t) = \int_0^\infty P_\tau(T_2) e^{-t/T_2} f(T_2) dT_2 + \epsilon(t). \quad (1)$$

The relaxation time T_2 is the characteristic time corresponding to loss of coherence by protons in hydrocarbons or water present in pores of a rock or in the bulk fluid. The corresponding non-negative amplitude $f(T_2)$ is the unknown distribution of T_2 relaxation times and $\epsilon(t)$ denotes additive, white, Gaussian noise with known statistics. In low-field measurements (as it is assumed in this paper) the relaxation times are essentially due to the surface-to-volume ratio of the pores so that, physically, the T_2 distribution corresponds to a pore size distribution where longer times represent larger pores [4]. In addition to the pore size, the T_2 distribution is also a function of the type of fluids present in the sample. The function $P_\tau(T_2)$ is assumed to be known and referred to as the polarization factor and determined either by the measurement physics (corresponding to different pulse sequences) and/or tool physics (various operational conditions). For example,

$$P_\tau(T_2) = \begin{cases} 1 & \text{CPMG pulse sequence with full polarization} \\ 1 - 2e^{-\tau/T_2} & \text{inversion recovery — CPMG pulse sequence} \\ 1 - e^{-\tau/T_2} & \text{saturation recovery — CPMG pulse sequence} \end{cases}$$

where τ is a function of pre-polarization time and longitudinal relaxation T_1. In downhole applications, the function $P_\tau(T_2)$ is a complex function of the tool geometry (such as length of the magnet and design of the RF antenna) and other operational constraints. In these applications, it is often well-fit by a polynomial function.

Traditionally, assuming $P_\tau(T_2)$ is known, an inversion algorithm is used to estimate the distribution of relaxation times $f(T_2)$ in Eq. (1) from the measured data $G(t)$ [5]. Next, linear functionals of the estimated $f(T_2)$ are used to estimate the petro-physical or fluid properties. For example, the area under the T_2 distribution is interpreted as the porosity of the rock. Often, based on lithology, a threshold T_2 is chosen as the cut-off characteristic time separating

* Corresponding author.
E-mail address: LVenkataramanan@slb.com (L. Venkataramanan).

1090-7807/$ - see front matter © 2013 Elsevier Inc. All rights reserved.
http://dx.doi.org/10.1016/j.jmr.2012.12.009

fluid bound to the pore surface and fluid that is not bound to the pore surface and can flow more easily. For example, in sandstones, relaxation times smaller than 33 ms have been empirically related to bound fluid volume. The remaining relaxation times correspond to free fluid volume. The mean of the distribution, $\langle \ln(T_2) \rangle$, is empirically related to either rock permeability and/or to hydrocarbon viscosity. The width of the distribution, $\sigma_{\ln(T_2)}$, provides a qualitative range of the distribution of pore sizes in the rock. Moments of relaxation time or diffusion are often related to rock permeability and/or hydrocarbon viscosity [6–11]. Similar properties can be obtained from linear functionals computed from two-dimensional diffusion-relaxation data or $T_1 - T_2$ relaxation data [12–14].

In this paper, we describe a method based on integral transforms that allows the direct computation of linear functionals of $f(T_2)$ from the measured magnetization data without involving an intermediate computation of the full distribution $f(T_2)$, which would require the inversion of an ill-conditioned, non-linear problem (see, e.g., [15]). Examples of linear functionals include areas and moments of relaxation time T_2. More complicated linear functionals can also be obtained by combining simpler ones by means of a convolution as shown later in this paper. This allows, for example, to find the moments of a specified region of the T_2 distribution. (see [22] for a classical treatment of the estimation of linear functionals and its applications to resolution limits in inverse problems).

This paper is organized as follows. In Section 2, we describe the estimation of moments and areas from integral transforms. We start with a brief review in Section 2.1 of a previous work by the authors [16] where the Mellin transform was used to obtain the μ-th moment of T_2 from fully polarized magnetization data. Then we describe an analogous method to estimate tapered areas of the T_2 distribution. In Section 2.2 these techniques are then extended to partially polarized measurements which is important in certain applications where there is not enough time to polarize the samples completely. Section 2.3 proposes some techniques to estimate other linear functionals of the T_2 distribution that are of interest in petrophysical analysis. Finally, Section 3 demonstrates the performance of the method on simulated data for typically assessed petrophysical properties.

2. Parameter estimation using integral transforms

The integral transform of the data $G(t)$ is denoted by $\mathcal{L}\{G(t)\} = A$, and is defined by

$$\mathcal{L}\{G(t)\} = A \equiv \int_0^\infty k(t)G(t)dt. \tag{2}$$

From Eqs. (1) and (2),

$$A = \int_0^\infty k(t)G(t)dt = \int_0^\infty K(T_2)P_\tau(T_2)f(T_2)dT_2 \tag{3}$$

where the functions $k(t)$ and $K(T_2)$ form a Laplace-transform pair, with

$$K(T_2) \equiv \int_0^\infty k(t)e^{-t/T_2}dt. \tag{4}$$

From the right-hand side of Eq. (3), for a desired linear transformation $K(T_2)$ in the T_2 domain, our objective is to construct a kernel $k(t)$ in the time-domain satisfying Eq. (4). In turn, from Eq. (2), the scalar product of $k(t)$ with the measured data allows direct computation of A, the parameter of interest.

This is illustrated in Fig. 1 with an example. The solid traces show the measured CPMG data $G(t)$ and its corresponding and unknown distribution $f(T_2)$. The dashed trace in Fig. 1(B) indicates the desired tapered transition $K(T_2)$ for computing the tapered area of the T_2 distribution (this is the area obtained from applying a tapered cut-off to the T_2 distribution) which can be used, e.g., to find the bound fluid volume in certain applications [17]. The kernel $k(t)$ corresponding to this tapered function $K(T_2)$ is shown in dashed line in Fig. 1(A). This function $k(t)$ was found using the methods described later in this paper. A scalar product of $k(t)$ with

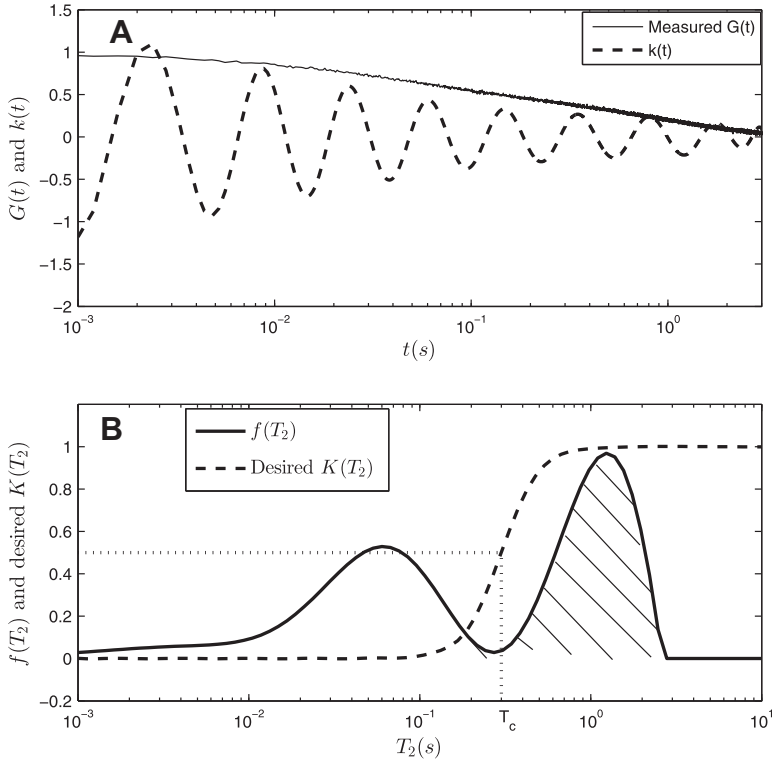

Fig. 1. The solid trace shows the measured data $G(t)$ in (A) and the underlying unknown relaxation distribution $f(T_2)$ in (B). Given a desired linear functional $K(T_2)$ (dashed trace) in (B), our objective is to estimate a kernel $k(t)$ such that the scalar product of $k(t)$ with the measured data directly provides parameter A (in this case the shaded area).

$G(t)$ directly provides the tapered area A. Since this approach does not involve solving for $f(T_2)$ and then estimating $\int_0^\infty K(T_2)f(T_2)dT_2$, it is more straight-forward and not susceptible to the subjectivity of traditional algorithms.

For a desired $K(T_2)$, when the function $k(t)$ exists analytically or can be computed numerically, the parameter A is obtained from Eq. (2). However, the function $k(t)$ may not exist $\forall\, K(T_2)$. When it exists, it may also have infinite energy which can be related to infinite uncertainty in the estimated parameter A leading to instability in computing the parameter. Thus, the integral transform approach have the advantage of being able to provide insight into what linear functionals of the T_2 distribution can be directly estimated from the data $G(t)$ and are stable in the context of providing low uncertainty in A.

The uncertainty in A can be quantified as a function of the signal-to-noise ratio (SNR) in the measured data. Let σ_ϵ denote the standard deviation of the additive white Gaussian noise in the data. Eq. (3) can be computed in the discrete-time domain as

$$A = t_E \sum_{i=0}^{N} k(it_E)G(it_E) \tag{5}$$

where t_E denotes the sampling time or echo spacing and N represents the number of samples (typically N is between 1000–4000). Therefore,

$$\sigma_A^2 = \sigma_\epsilon^2 t_E \left[\sum_{i=0}^{N} k^2(it_E)t_E\right]. \tag{6}$$

Eq. (6) shows that when the kernel $k(t)$ is square integrable, i.e., $k(t)$ has finite energy E, where $E = \int_0^\infty k^2(t)dt$, then the uncertainty in A is always finite and directly related to the uncertainty in the measurement.

2.1. Completely polarized measurements

When the measurements are completely polarized then the polarization factor is

$$P_\tau(T_2) = 1\ \forall\ \tau, T_2 \tag{7}$$

so that the expression for the magnetization decay in (1) reduces to

$$M(t) = \int_0^\infty e^{-t/T_2} f(T_2)dT_2. \tag{8}$$

Here we use $M(t)$ instead of $G(t)$ to emphasize the fact that the measured data is fully polarized.

2.1.1. Moments of relaxation time $\langle T_2^\omega \rangle$

In this case, the ω-th moment of T_2, denoted by $\langle T_2^\omega \rangle$ can be obtained using the Mellin operator, [16]

$$\langle T_2^\omega \rangle = \frac{(-1)^n}{\phi\Gamma(\mu)} \int_0^\infty t^{\mu-1}\left[\frac{d^n M(t)}{dt^n}\right]dt, \tag{9}$$

$$\omega = \mu - n, \quad \text{with} \begin{cases} n = 0, & \text{if } \omega > 0, \\ n = [-\omega] + 1 & \text{otherwise} \end{cases} \tag{10}$$

where ϕ is the area under the T_2 distribution, $\Gamma()$ represents the Gamma function and $[\omega]$ indicates the integral part of the number ω. The contribution of variable ω is in two parts: a real number μ and an integer n where the mathematical operator $t^{\mu-1}$ operates on the n-th derivative of the data (see [16] for more details and benchmarks).

2.1.2. Tapered areas

Tapered or sharp areas under the T_2 distribution are often related to fluid or petro-physical properties [3,17]. The distribution of relaxation times is often seen to be reflective of the distribution of pore sizes in the rock, which varies from a few hundred microns to a few mm. Small pores are associated with short relaxation times. A cut-off relaxation T_c (see Fig. 1) computed from laboratory data is the characteristic time separating fluids in small and large pores. Due to higher capillary pressure, a larger differential pressure is required to withdraw fluids in small pores. Thus, T_c is often viewed as the relaxation time separating the fraction of fluid bound to the rock from the fraction that can flow more readily. In sandstones, this characteristic time constant is on the order of 33 ms [17].

In this sub-section, we provide linear kernels $k(t, T_c)$ such that the equivalent transforms $K(T_2, T_c)$ corresponds to tapered Heaviside functions. Thus, for a given $K(T_2, T_c)$, the tapered area can be computed from an integral transform of the measured data using the equivalent kernel $k(t, T_c)$. We are particularly interested in integral transforms that:

- can select portions of the T_2 spectrum,
- have a specific cutoff, and
- are analytically tractable.

The functions $k(t, T_c)$ and $K(T_2, T_c)$ should satisfy the following properties:

1. The function $k(t, T_c)$ should exist $\forall\ t$ and $K(T_2, T_c)$ should exist $\forall\ T_2$.
2. Based on the underlying petrophysics, it is desirable that $K(T_2, T_c)$ be monotonic between 0 and 1 (on the y-axis), with

$$K(T_2, T_c)|_{T_2=0} = 0 \tag{11}$$

$$\lim_{T_2\to\infty} K(T_2, T_c) = 1 \tag{12}$$

$$K(T_2, T_c)|_{T_2=T_c} = 0.5. \tag{13}$$

3. To be able to provide arbitrarily sharp cut-offs in the T_2 domain, it should be possible to adjust the slope m in the $\log(T_2)$ space of the transition region, with

$$m \equiv \frac{dK(T_2, T_c)}{d\log T_2}|_{T_2=T_c}. \tag{14}$$

In most oilfield applications, the desired slope varies from $m = 0.4$ for gradual tapered cut-offs to $m = 4$ for sharp cut-offs [17].

A set of integral transforms that satisfy these properties are summarized in Table 1. For ease of reference, we have suggested names for the transforms based on the kernel $k(t)$. For example, the sinc transform of the measured data can directly provide tapered area with a finite energy (and uncertainty in A). The energy for the Haar and Sine transforms is infinite, implying infinite uncertainty in the estimated area. This energy can be decreased by several methods. One such method involves multiplication of the kernel $k(t)$ by an exponential decaying signal in the time domain. A second method involves restricting the integral transform to a finite time-period. Both methods decrease the energy considerably while also reducing the slope in the transition region. For example, as shown in Table 1, the Haar transform (HT) (row 3) and the Sine transform (ST) (row 4) has infinite energy. On the other hand, the energy of an exponential Haar transform (EHT) (row 5) and the exponential Sine transform (EST) (row 6) is finite. The parameters of EHT and EST that will provide the same uncertainty as the sinc transform are provided in the table.

For the Heaviside function $K(T_2, T_c) = 1$ for $T_2 > T_c$ (corresponding to sharp cut-offs), an exact mathematically equivalent $k(t, T_c)$ does not exist. Approximations exist for $k(t, T_c)$ such that asymptotically, the equivalent $K(T_2, T_c)$ converges to the Heaviside function. However, functions $k(t, T_c)$ grow exponentially with time, leading to infinite energy and uncertainty in A. Thus, there is a trade-off

Table 1
Tables of integral transform used in the estimation of tapered areas from fully polarized measurements.

$K(T_2, T_c)$	Parameters	$k(t, T_c)$	E	m	Name of transform
$\frac{2}{\pi}\tan^{-1}(\alpha T_2)$	$\alpha = \frac{1}{T_c}$	$\frac{2}{\pi}\frac{sin(\alpha t)}{t}$	$\frac{2}{\pi T_c}$	0.32	Sinc
$\frac{T_2}{\alpha}\tanh\left(\frac{\alpha}{T_2}\right)$	$\alpha = \frac{T_c}{0.52219}$	$\frac{1}{\alpha}(-1)^n$ $2n\alpha < t < 2(n+1)\alpha$	∞	0.42	Haar
$\frac{\alpha^2}{\alpha^2 + \frac{1}{T_2^2}}$	$\alpha = \frac{1}{T_c}$	$\alpha \sin(\alpha t)$	∞	0.5	Sine
$\frac{C}{\gamma}\tanh(\alpha\gamma)$	$C = \frac{0.7213}{T_c}$	$C(-1)^n e^{-\beta t}$	$\frac{2}{\pi T_c}$	0.35	Exponential
	$\alpha = (1.572)T_c$	$2n\alpha < t < 2(n+1)\alpha$			Haar
	$\beta = \frac{0.4087}{T_c}$				
	$\gamma = \frac{1}{T_2} + \beta$				
	$\alpha = \sqrt{4E\beta - \beta^2}$				
$\frac{\alpha^2 + \beta^2}{\alpha^2 + \gamma^2}$	$\beta = \frac{1}{T_c^2\left(4E - \frac{2}{T_c}\right)}$	$\frac{\alpha^2 + \beta^2}{\alpha} e^{-\beta t} sin(\alpha t)$	$\frac{2}{\pi T_c}$	0.3	Exponential
	$\gamma = \frac{1}{T_2} + \beta$				Sine

between finite uncertainty in A and sharpness of transition in the T_2 domain. The sharper the desired transition, the larger the energy E of the equivalent kernel, leading to larger uncertainty in A.

From Eq. (6), a desired and finite uncertainty in the estimated area σ_A can be translated to a desired and finite energy in the kernel. This finite energy can be achieved by suitable choice of parameters of the transform satisfying both the energy criteria as well as Properties 1–3 described above.

Fig. 2 illustrates the exponential Haar transform for 3 different values of the parameter T_c. Subplot A shows the time domain while subplot B shows the T_2 domain of the same transform.

Thus the integral transform method is appropriate for the estimation of bound and free fluid volumes as long as a tapered cut-off is applicable. This, in turn, depends on the type of formation. A comparison between sharp and tapered cut-offs can be found in the work by Kleinberg and Boyd [17].

2.2. Partially polarized measurements

Consider the partially polarized data with

$$P_\tau(T_2) = 1 - e^{-\tau/T_2} \tag{15}$$

where $\tau = T_w/r, r = \left\langle \frac{T_1}{T_2} \right\rangle$ and T_w is the wait time. This polarization factor plays an important role in saturation–recovery-CPMG pulse sequences and is often used in downhole oilfield applications. We show below that the integral transform approach that was developed on fully polarized data can be applied to partially polarized data as well. From Eqs. (1) and (15)

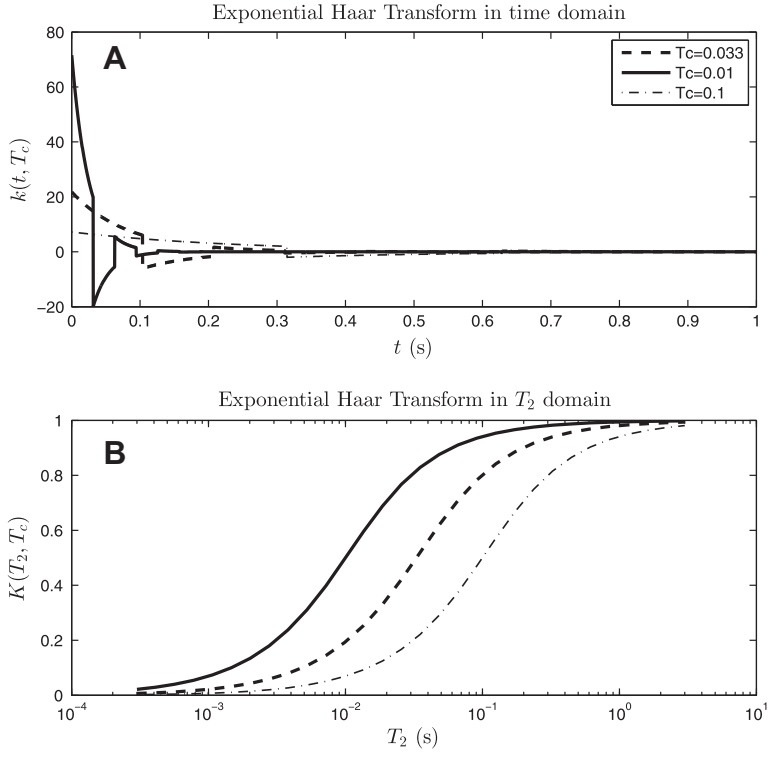

Fig. 2. (A) Shows the exponential Haar transform in time domain for different values of T_c. (B) Shows the exponential Haar transform in T_2 domain.

$$G(t) = \int_0^\infty e^{-t/T_2} f(T_2) dT_2 - \int_0^\infty e^{-(t+\tau)/T_2} f(T_2) dT_2 \tag{16}$$

Eq. (16) can then be cast as follows

$$G(t) = M(t) - M(t+\tau) \tag{17}$$

For a finite time t we have

$$\lim_{N\to\infty} M(t+N\tau) = 0. \tag{18}$$

Therefore

$$\sum_{n=0}^{N-1} G(t+n\tau) = M(t) - M(t+N\tau) \tag{19}$$

For a finite time t and in the limit $N \to \infty$, we get

$$M(t) = \sum_{n=0}^{\infty} G(t+n\tau). \tag{20}$$

Therefore, if τ is either known or estimated, the fully polarized data $M(t)$ can be reconstructed using Eq. (20) from the measured data $G(t)$. Integral transforms can be applied to $M(t)$ to directly estimate linear functionals of $f(T_2)$.

In logging applications the measuring tool is moved from the bottom of the well to the top while measuring. Because some of the wells can be rather deep, the time that is spent at each sampling depth is very limited. This has the effect of measuring underpolarized samples which are modeled by a more complicated polarization factor $P_\tau(T_2)$. The specific shape of this factor in logging tools depends on the design of the instrument such as the magnetic profile of the magnet, the speed of logging as well as acquisition parameters such as number of measurements, and echo spacing. In general, this function is a constant for small values of T_2 and decays for large values of T_2. The rate of decay is related to the speed of the tool. Faster speeds implies less time polarizing the samples so that only small pores in the rock (associated with small values of T_2) are fully polarized. Larger pores (associated with large values of T_2) are under polarized. This behavior dictates how fast the polarization factor decays.

For simplicity, we have ignored the subscript τ in the polarization term in this sub-section. In these applications, we have found that over a range of factors, $P(T_2)$ is well represented by

$$P(T_2) \simeq \frac{1}{\sum_{k=0}^{\infty} a_k e^{-b/T_2}} \tag{21}$$

where a_k and b are coefficients that need to be estimated for a given polarization factor $P(T_2)$. Extensive testing have found that Eq. (21) is a good fitting function for a wide range of parameters (like, e.g., logging speed). The top plot in Fig. 3 illustrates the polarization factor for different logging speeds and the corresponding fit using (21). The bottom plot shows, for each speed, the values for the parameters a_k and b. Also note that the polarization factor of the previous subsection is a special case of (21) for $b = \tau$ and $a_k = 1 \; \forall \, k$.

2.3. Other types of integral transforms

The integral transforms described so far can also be combined in the time domain to estimate other parameters. For example, the moments of a specified region of the T_2 distribution can be computed by using a kernel computed as the convolution of the Mellin operator and the Exponential Haar transform. Consider two different integral transforms of the measured data, where kernel $k(t)$ in (2) is represented by $k_1(t)$ and $k_2(t)$, respectively,

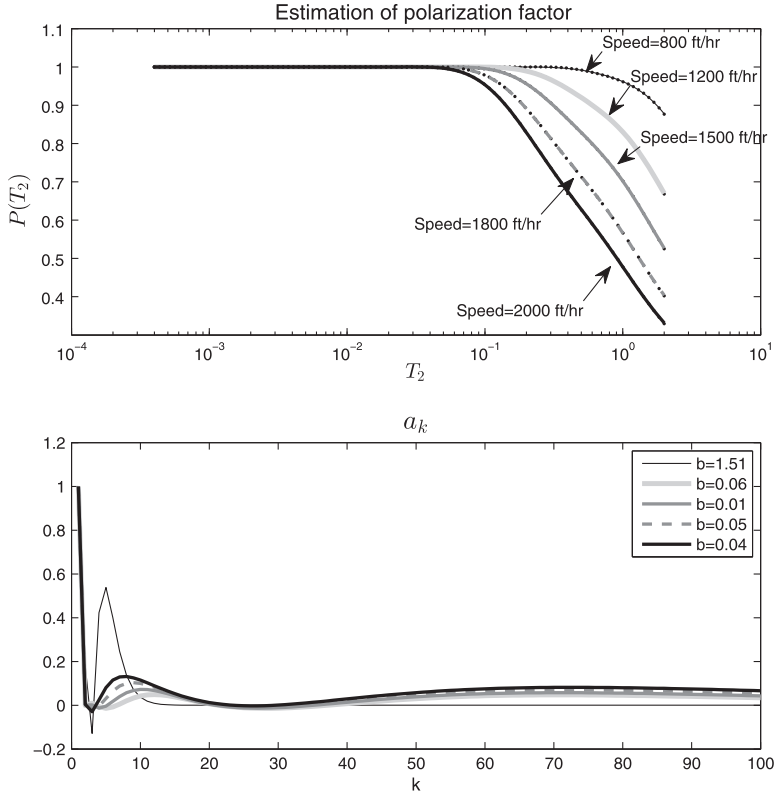

Fig. 3. The polarization factor in logging tools is a complex function of tool geometry, operational constraints such as logging speed and pulse sequence. In a number of circumstances, such as shown in this example, at logging speeds varying from 800–2000 ft/h, the fit (solid line) from Eq. (21) fits the polarization factor (in dots) very well. The bottom plot shows the coefficients a_k obtained from the fit.

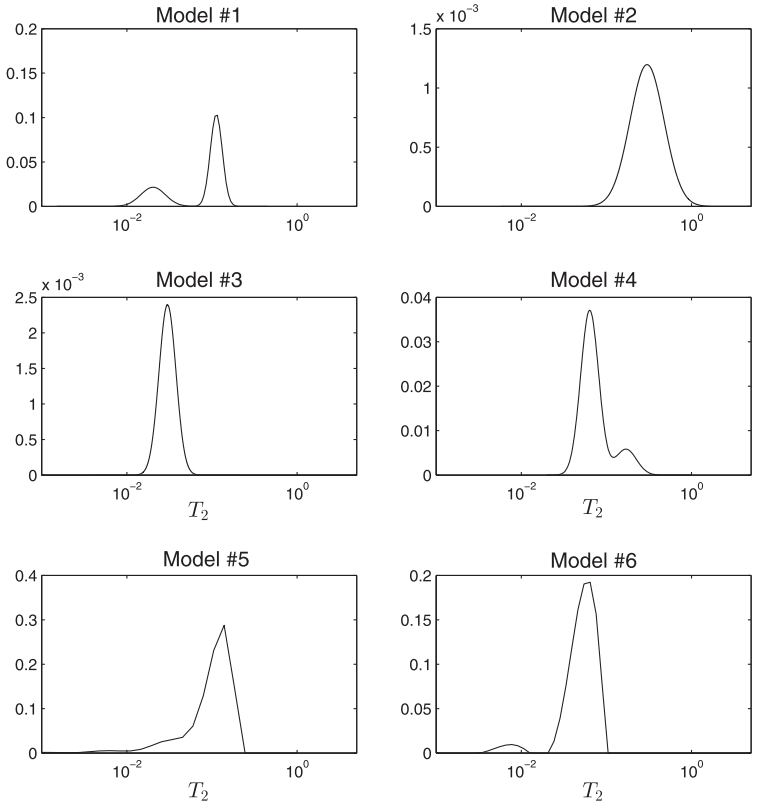

Fig. 4. Test T_2 distributions used in the numerical experiments.

$$A_1 = \int_0^\infty k_1(t)G(t)dt = \int_0^\infty K_1(T_2)P_\tau(T_2)f(T_2)dT_2 \quad (22)$$

$$A_2 = \int_0^\infty k_2(t)G(t)dt = \int_0^\infty K_2(T_2)P_\tau(T_2)f(T_2)dT_2. \quad (23)$$

Here, the functions $K_1(T_2)$ and $K_2(T_2)$ correspond to different linear functionals.

Our interest is in evaluation of A_3 defined as

$$A_3 = \int_0^\infty K_3(T_2)P_\tau(T_2)f(T_2)dT_2, \quad (24)$$

where

$$K_3(T_2) \equiv K_1(T_2)K_2(T_2). \quad (25)$$

From the convolution property for the Laplace transform (see, e.g., [18]) we find that the required time-domain function $k_3(t)$ is given by the convolution

$$k_3(t) = \int_0^t k_1(\tau)k_2(t-\tau)d\tau. \quad (26)$$

Thus, A_3 can be computed from

$$A_3 = \int_0^\infty k_3(t)G(t)dt. \quad (27)$$

This property implies, for example, that the moments of a specified region of the T_2 distribution can be computed by integral transforms of the measured data, using a kernel obtained as a convolution of the kernel of the Mellin operator and the kernel of the Exponential Haar transform.

It is possible that $K(T_2)$ is not well approximated by a closed form expression or an analytical $k(t)$ does not exist for a specified $K(T_2)$. In this case, $k(t)$ can be computed numerically as follows. For example, suppose the desired $K(T_2, T_c)$ is shown in the dotted trace in Fig. 1(B). A numerical least squares approximation to $k(t, T_c)$ can be obtained using singular value decomposition (SVD), with

$$\tilde{k}(t) \approx V_n \Sigma_n^{-1} U_n^T K(T_2). \quad (28)$$

Here matrices U, Σ and V are obtained by the SVD of the kernel e^{-t/T_2} and n refers to the number of significant singular values. Fig. 1(A) shows the $\tilde{k}(t)$ obtained using Eq. (28).

Table 2
Acquisition parameters for models #1–#6.

Model #	N	τ (s)
1	5000	0.27
2	5000	1
3	2000	0.1
4	8000	0.27
5	8000	1.5
6	5000	0.15

3. Simulation results

As an illustration of the use of the integral transforms described in the previous sections, we consider the six models with T_2 distributions shown in Fig. 4. Models 5 and 6 were derived from the stretched exponential (Kohlrausch function),

$$M_{se}(t) = e^{-(t/T_0)^\alpha}$$

a common function used to represent magnetization decay [19]. Model 5 used $\alpha = 0.85$ and $T_0 = 0.1$ while model 6 used $\alpha = 0.9$ and $T_0 = 0.05$.

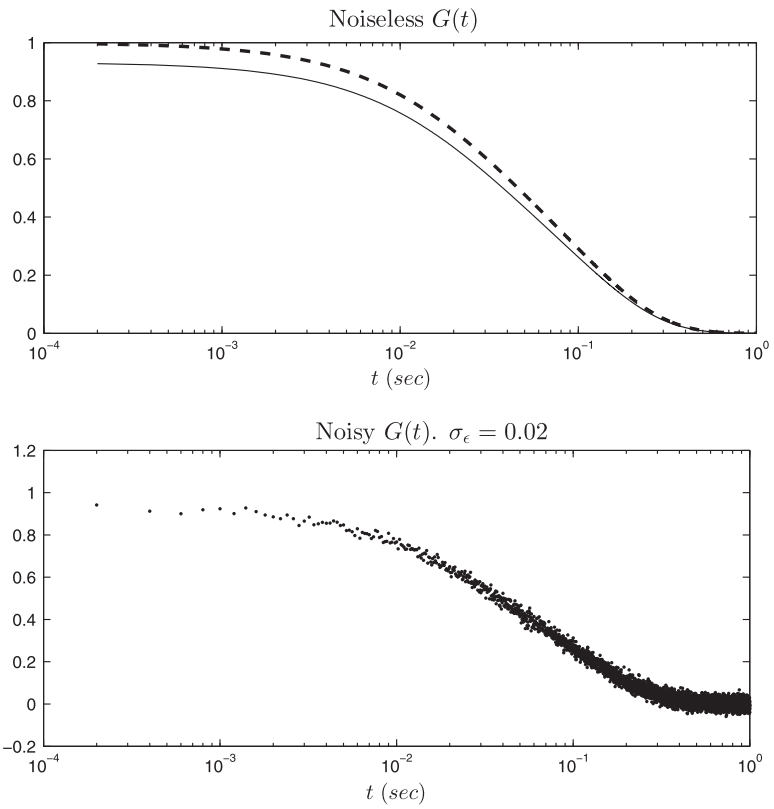

Fig. 5. Model #1 magnetization decay $G(t)$ with and without noise.

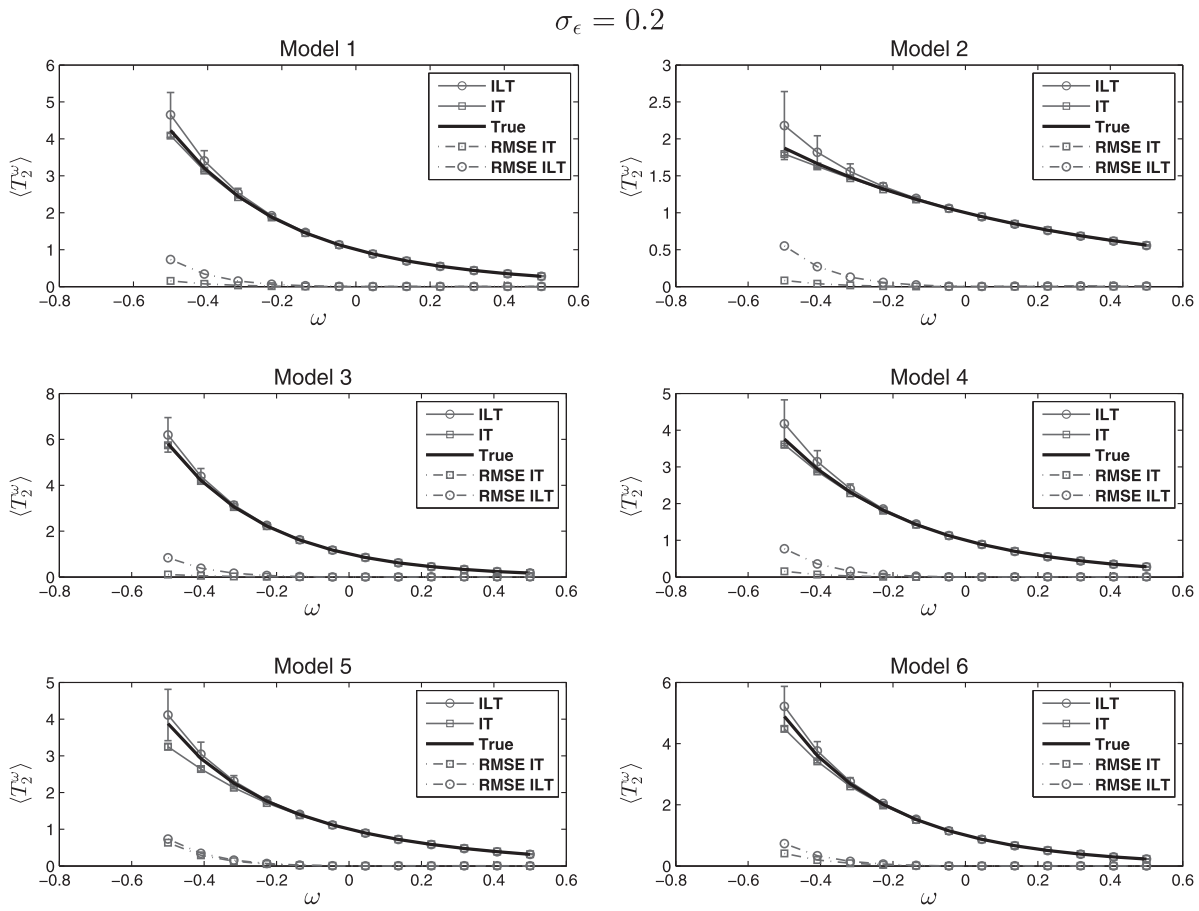

Fig. 6. Mean and standard deviation of the estimated moments using the inversion of the T_2 distribution (ILT) and the integral transform (IT) described in this paper. $\sigma_\epsilon = 0.02$.

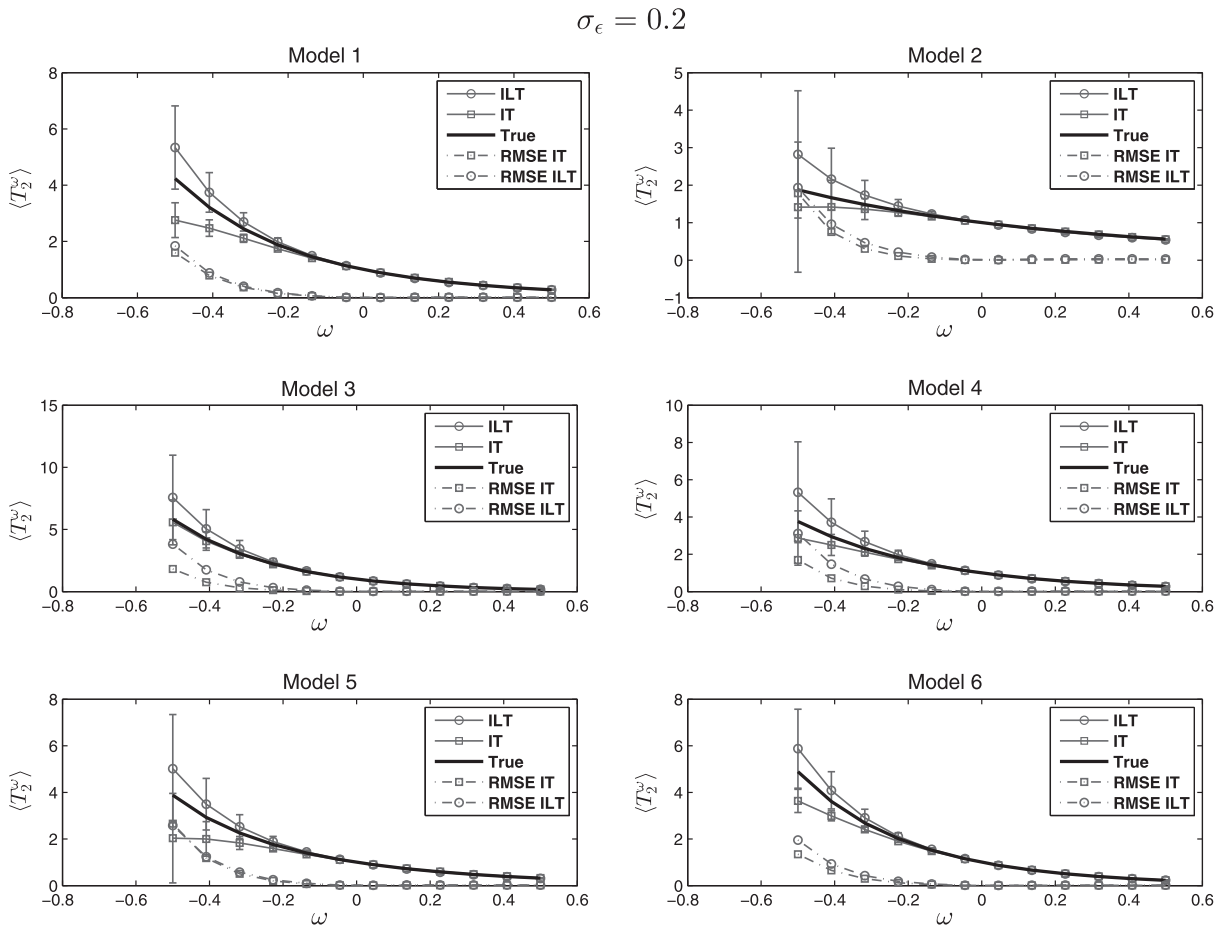

Fig. 7. Mean and standard deviation of the estimated moments using the inversion of the T_2 distribution (ILT) and the integral transform described in this paper (IT). $\sigma_\epsilon = 0.2$.

Table 3
Mean (μ), standard deviation (σ), and root mean square error (rmse) in the estimated tapered areas using ILT and IT. $\sigma_\epsilon = 0.02$.

Model	True	Area IT		Area ILT	
		$\mu \pm \sigma$	rmse	$\mu \pm \sigma$	rmse
1	0.683	0.683 ± 0.00138	0.00137	0.685 ± 0.00147	0.00252
2	0.928	0.925 ± 0.00189	0.00363	0.929 ± 0.00177	0.00234
3	0.471	0.471 ± 0.00172	0.00176	0.0474 ± 0.0066	0.00727
4	0.722	0.721 ± 0.0015	0.00178	0.722 ± 0.00202	0.00202
5	0.761	0.759 ± 0.00129	0.00185	0.761 ± 0.00126	0.00126
6	0.668	0.669 ± 0.00181	0.00187	0.67 ± 0.00192	0.00273

Table 4
Mean (μ), standard deviation (σ), and root mean square error (rmse) in the estimated tapered areas using ILT and IT. $\sigma_\epsilon = 0.2$.

Model	True	Area IT		Area ILT	
		$\mu \pm \sigma$	rmse	$\mu \pm \sigma$	rmse
1	0.683	0.686 ± 0.013	0.0134	0.694 ± 0.0131	0.0167
2	0.928	0.925 ± 0.0167	0.0169	0.943 ± 0.0158	0.0219
3	0.471	0.475 ± 0.0159	0.0164	0.491 ± 0.0475	0.0515
4	0.722	0.717 ± 0.0146	0.0155	0.719 ± 0.0161	0.0163
5	0.761	0.757 ± 0.0127	0.0132	0.753 ± 0.0125	0.0143
6	0.668	0.671 ± 0.0162	0.0164	0.678 ± 0.0186	0.0211

In all cases the area under the distribution is 1. For each of these models we generated the magnetization decay $G(t)$ using the expression

$$G(t) = \int_0^\infty (1 - e^{-\tau/T_2}) e^{-t/T_2} f(T_2) dT_2 + \epsilon(t) \tag{29}$$

where ϵ represents white Gaussian noise with standard deviation $\sigma_\epsilon = 0.02$ and 0.2 giving a SNR of 50 (lab measurements) and 5 (field measurements), respectively. For all cases the time t was sampled at 200μs. The number of samples (N) as well as the values of the parameter τ in (29) are given in Table 2. The values of τ shown in the table are typical for imperfectly polarized measurements acquired down-hole.

In order to gather statistics we process each case (for each model and noise standard deviation) 100 times with different realizations of noise $\epsilon(t)$. Take, for example, the T_2 distribution for model #1. The top plot in Fig. 5 shows, in solid black line, the simulated magnetization decay $G(t)$ without noise. In the same plot we include, as reference, the magnetization decay assuming complete polarization (black dotted line). The bottom plot shows the noisy measurements after adding white Gaussian noise with standard deviation $\sigma_\epsilon = 0.02$.

It is also important to mention that the first magnetization measurements happens at time $t = 200\,\mu s$ and, therefore, in order to capture the part of the integral in (2) between 0 and 200 μs it is necessary to have, at least, an estimate of $G(0)$ (see [16] for a detailed description of this issue). In this section we calculate the $G(0)$ with a method described in [20] based on applying the Mellin transform to the Fourier transform of the measured magnetization decayed in the $\sqrt{t}$ domain. This algorithm was found to give good results for T_2 distributions with T_2 components larger than the echo spacing.

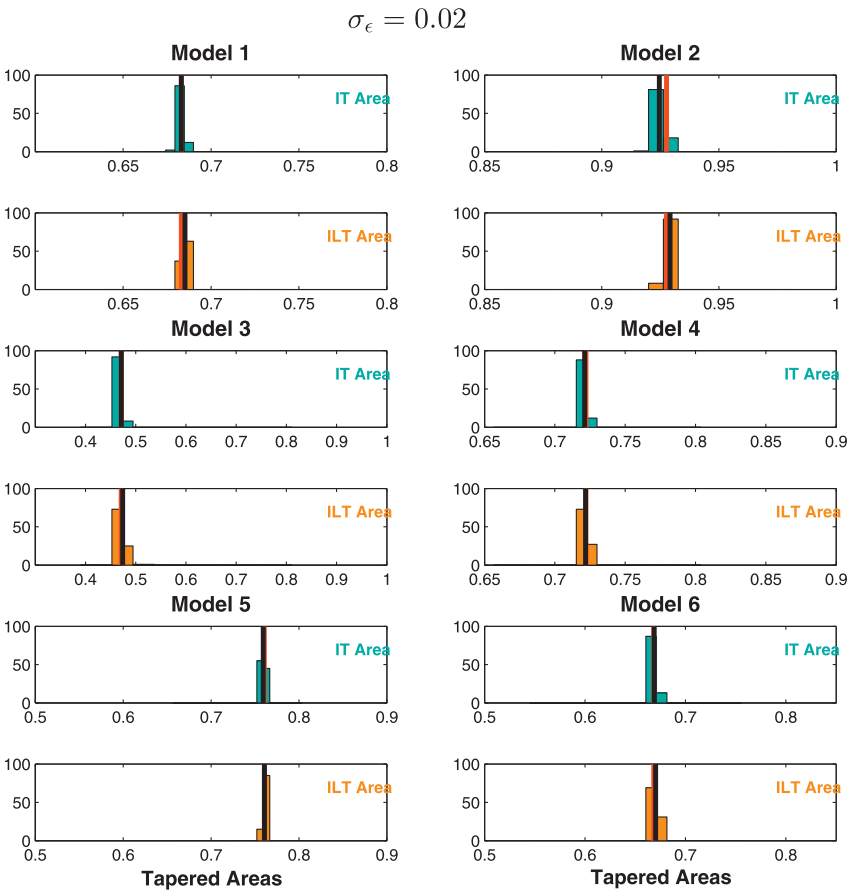

Fig. 8. Histograms of the estimated areas using ILT (orange) and using EHT (green). The black line represent the mean value and the red corresponds to the true value. SNR = 50.

3.1. Computation of moments

Sections 2.1.1 and 2.2 described the estimation of the moments from imperfectly polarized measurements using the integral transform method. In this section we illustrate the use of these equations. For reference we also estimate the moments from the estimated T_2 distribution with a regularization parameter selected according the Butler, Reeds, Dawson algorithm (BRD) [21]. A moment of order ω is calculated from the estimated and normalized T_2 distribution $\hat{f}_n(T_2)$ by the expression

$$\langle T_2^\omega \rangle = \frac{1}{\phi} \int_0^\infty T_2^\omega \hat{f}_n(T_2) dT_2$$

The moments are estimated for each of the 100 realizations of white Gaussian noise. From these estimates we calculate statistics like the mean, standard deviation, and root mean square error (rmse). The rmse of an estimate $\hat{x}$ of x is defined as

$$rmse = \sqrt{\langle (\hat{x} - x)^2 \rangle}.$$

Fig. 6 illustrates the statistics of the estimated moments for a noise standard deviation of 0.02. This level of noise represents good quality measurements as you would expect in a laboratory environment. The black line represents the true moments. The gray circled errorbars correspond to the mean and standard deviation of the estimated moments from the BRD T_2 distribution (ILT). The squared errorbars correspond to the mean and standard deviation of the moments estimated directly using the integral transform approach (IT). The dash lines indicate the rmse for each case. The results for models #1–#4 and #6 show that the moments estimated using IT have less bias, standard deviation, and rmse than the estimates from ILT. For model #5 the rmse was essentially the same for both methods.

For a high level of noise with $\sigma_\epsilon = 0.2$ (see Fig. 7) the performance of the IT algorithm is still considerable better for models #3 and #4. For models #1 and #5, the performance, as measured by the rmse, was essentially the same (of course the tradeoff between bias and variance for the two methods is different). For model #2 the performance of IT was slightly better or equal as ILT for most moments. For the rest of the model we found considerable improvement in the rmse when using IT over ILT.

3.2. Computation of tapered areas

Now consider the estimation of tapered areas using the exponential Haar transform as defined in Table 1 with $T_c = 33$ ms. Again we generated 100 realizations of white Gaussian noise and for each realization, noise standard deviation, and model we estimate the tapered area using the exponential Haar integral transform and, for reference, we also calculate the tapered area from the T_2 distribution as was done in the previous section.

Tables 3 and 4 summarizes the results for a noise standard deviation of $\sigma_\epsilon = 0.02$ and $\sigma_\epsilon = 0.2$, respectively. For high SNR both the IT and ILT estimates perform essentially the same. For low SNR, however, the IT estimates performed better (lower rmse). The same conclusions are found by looking at the histograms of the estimated areas using IT and ILT as shown in Figs. 8 and 9. The distance between the black and red line represent the bias in the

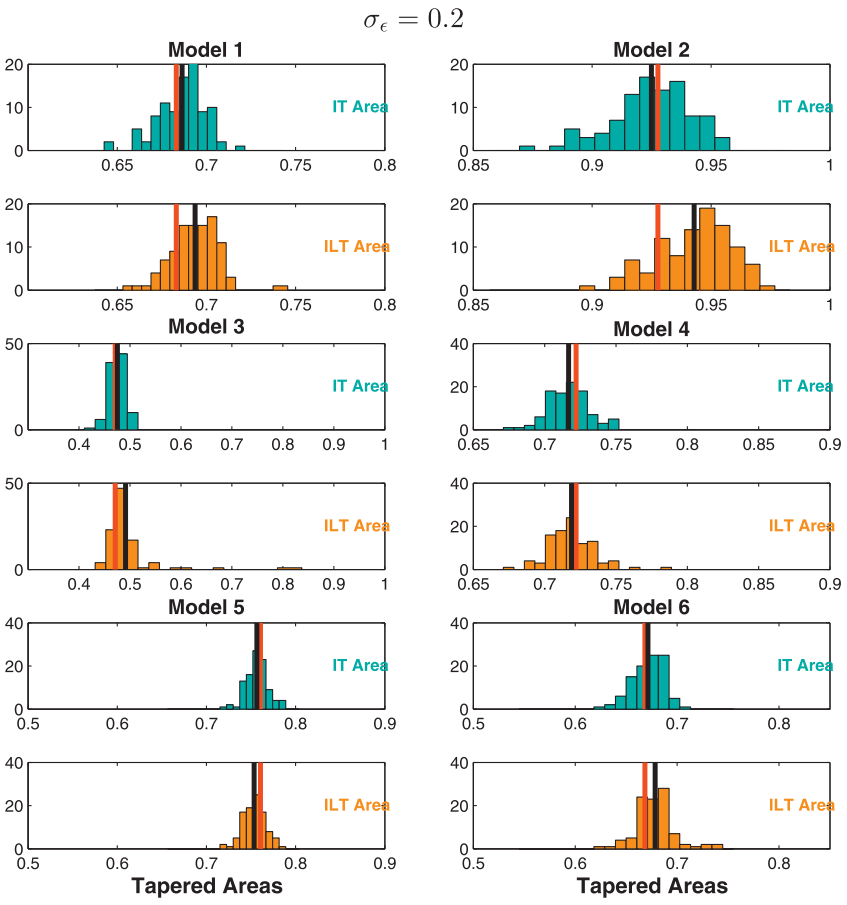

Fig. 9. Histograms of the estimated areas using ILT (orange) and EHT (green). The black line represent the mean value and the red corresponds to the true value. SNR = 5.

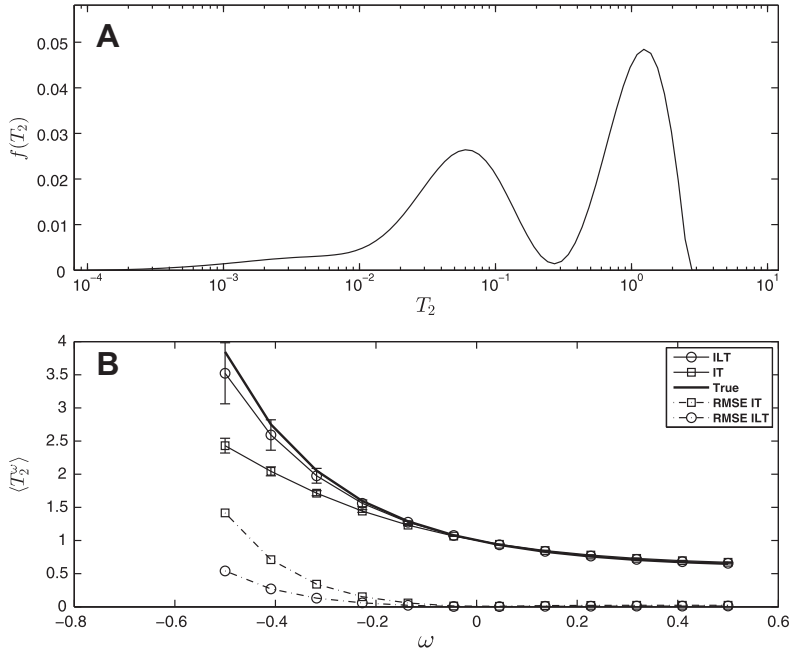

Fig. 10. The estimated moments for model #7 show the increased bias in the integral transform method when the T_2 distribution contains very short relaxation times of the order of the echo spacing and when the behavior of the magnetization decay between 0 and 200 μs has not been well characterized.

estimates while the spread of the histogram tells us about the variance. For the high SNR case the performance of the two methods was very similar. But for low SNR the IT estimates show a reduction in bias while keeping the variance at a similar level.

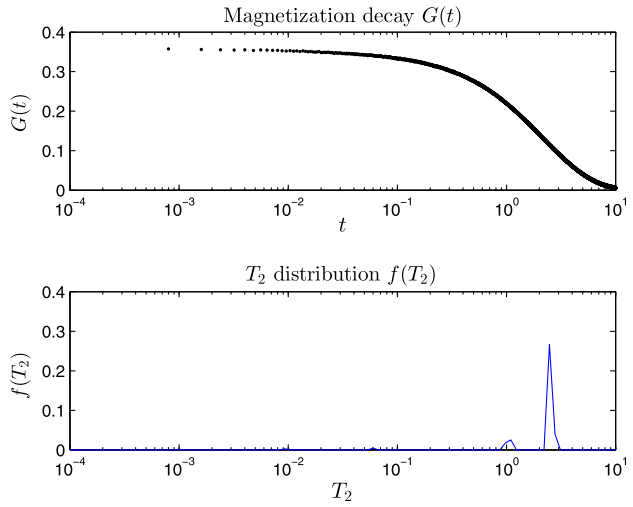

Fig. 11. Ground truth obtained from averaging 10 laboratory experiments for the same sample. Top plot shows the magnetization decay while the bottom plot shows the T_2 distribution.

3.3. Limitations

Models #1–#6 considered above have T_2 distributions with relaxation times significantly larger than the echo spacing of 200 μs. However, when the magnetization decay is on the order of the echo spacing then the integral transforms become biased. Consider, for example, model #7 with T_2 distribution shown in Fig. 10A. Because of the T_2 components of the order of the echo spacing, the magnetization decay is not well characterized in the region between 0 and 200 μs. Fig. 10B shows the estimated moments for a noise standard deviation of 0.02. The estimated moments using the integral transform have an increased bias with respect to the moments estimated using ILT. Also the rmse is considerably larger.

This limitation is being addressed by a new method which we will describe in a succeeding paper.

4. Experimental results

Finally, we tested the algorithm on experimental measurements. The difficulty with real measurements is the lack a ground truth to use as a reference in the calculation of the error (rmse). This is specially true for field measurements taken downhole in oil wells. Nevertheless, in order to get validation with real data we obtained laboratory results for a sample of doped water (water with salt). Ten experiments on the same sample were ran. This 10 magnetization measurements were combined to obtain a very high signal-to-noise ratio signal. This high quality measurement was processed to obtain the "ground truth" using ILT (see Fig. 11). Then the 10 individual measurements were processed with ILT and IT and compared to the ground truth.

Fig. 12 shows the mean, standard deviation, and rmse of the estimated moments using ILT (circles) and IT (squares) as well as the true moments (thick line). It was observed that for the negative order moments the integral transform approach provided considerably better estimates (less rmse, and bias) than ILT. For the positive order moments the performance was similar.

Since, as shown in Fig. 11, the T_2 distribution is mostly concentrated at values of T_2 larger than 1 s we estimate tapered areas with $T_c = 1s$. Both ILT and IT had an identical performance with a mean and standard deviation of the areas of 0.26 ± 0.0026.

5. Summary

We have described a novel method for computing linear functionals of the distribution function (e.g., moments and tapered areas) directly from the measured magnetization data without

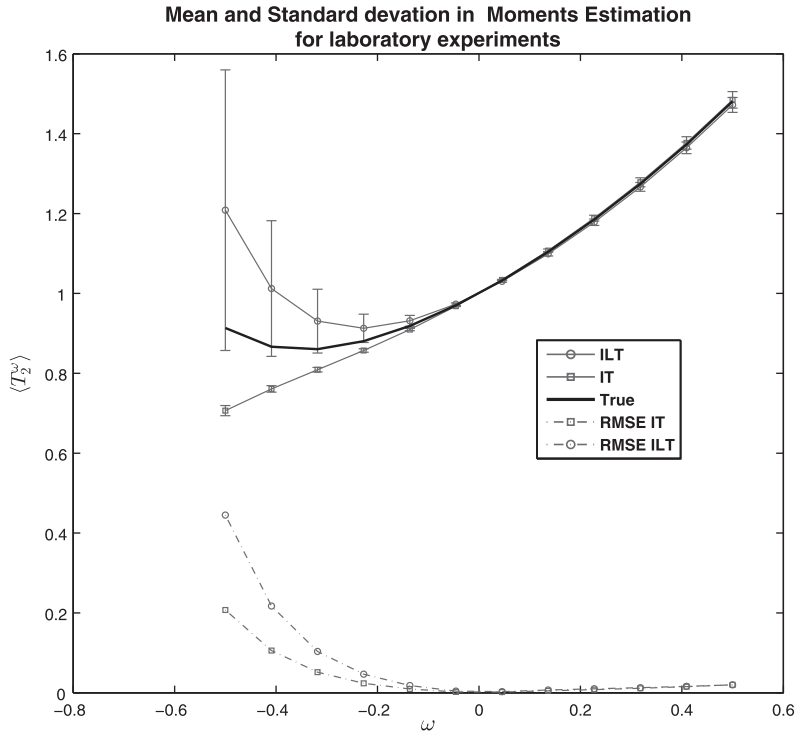

Fig. 12. Mean and standard deviation of the estimated moments using the inversion of the T_2 distribution (ILT) and the integral transform described in this paper (IT). Red curve represents the true moments.

the intermediate step of first estimating the distribution of relaxation times. This method involves a linear transform of the measured data using integral transforms. Different linear functionals of the distribution function can be obtained by choosing appropriate kernels in the integral transforms. Two main advantages of this method were discussed in this paper. First, as shown in the simulation and experimental results, the estimates from this new method are more accurate than the estimates obtained by inverting the distribution first. Second, the uncertainty in the linear functional can be obtained as a function of the SNR in the measured data. This approach can also be extended to multiple dimensions such as diffusion-relaxation measurements and can be applied to data obtained from a variety of pulse sequences including CPMG, inversion and saturation recovery, and diffusion editing, as well as pulse sequences often deployed down-hole.

References

[1] R.L. Kleinberg, C. Straley, W.E. Kenyon, R. Akkurt, S.A. Farooqui, Nuclear magnetic resonance of rocks: T_1 vs. T_2, SPE 26470 (1993) 553–563.

[2] M. Hurlimann, D. Griffin, Spin dynamics in grossly inhomogeneous dc and rf fields and application to NMR well logging, J. Magn. Reson. 143 (2000) 120–135.

[3] R.L. Kleinberg, Encyclopedia of Nuclear Magnetic Resonance: Chapter Well Logging, vol. 8, John Wiley, 1996.

[4] C. Straley, D. Rossini, H. Vinegar, P. Tutunjian, C. Morriss, Core analysis by low-field NMR, Log Anal. 38 (2) (1997) 84–94.

[5] D.P. Gallegos, D.M. Smith, A NMR technique for the analysis of pore structure: determination of continuous pore size distributions, J. Colloid Interface Sci. 122 (1) (1988) 143–153.

[6] G.C. Borgia, Borlotti, R.J.S. Brown, P. Fantazzini, A robust method for calculating geometric mean times from multiexponential relaxation data, using only a few data points and only a few elementary operations, Magn. Reson. Imaging 14 (1996) 895–897.

[7] G.C. Borgia, V. Bortolotti, R.J.S. Brown, P. Fantazzini, A method for approximating fractional power average relaxation times without inversion of multiexponential relaxation data, Magn. Reson. Imaging 16 (1998) 625–627.

[8] G.C. Borgia, R.J.S. Brown, P. Fantazzini, Estimates of permeability and irreducible water saturation by means of a new robust computation of fractional power average relaxation times, Magn. Reson. Imaging 16 (1988) 613–615.

[9] G.C. Borgia, R.J.S. Brown, P. Fantazzini, Different average NMR relaxation times for correlation with fluid-flow permeability and irreducible water saturation in water-saturated sandstones, J. Appl. Phys. 82 (9) (1997).

[10] D.E. Freed, Scaling laws for diffusion coefficients in mixtures of alkanes, Phys. Rev. Lett. 94 (2005) 067602.

[11] D.E. Freed, Dependence on chain length of NMR relaxation times in mixtures of alkanes, J. Chem. Phys. 126 (2007) 174502.

[12] M.D. Hürlimann, L. Venkataramanan, Quantitative measurement of two-dimensional distribution functions of diffusion and relaxation in grossly inhomogeneous fields, J. Magn. Reson. 157 (2002) 1–12.

[13] Y.-Q. Song, L. Venkataramanan, M.D. Hürlimann, M. Flaum, P. Frulla, C. Straley, $T_1 - T_2$ correlation spectra obtained using a fast two-dimensional Laplace inversion, J. Magn. Reson. 154 (2002) 1–8.

[14] D. Allen, S. Crary, R. Freedman, How to use borehole nuclear magnetic resonance, Oilfield Rev. (1997) 34–57.

[15] C.L. Epstein, J. Schotland, The bad truth about Laplace's transform, SIAM Rev. 50 (2008) 504–520.

[16] L. Venkataramanan, F.K. Gruber, T.M. Habashy, D.E. Freed, Mellin transform of CPMG data, J. Magn. Reson. 206 (2010) 20–31.

[17] R.L. Kleinberg, A. Boyd, Tapered cutoffs for magnetic resonance bound water volume, in: SPE Annual Technical Conference and Exhibition, Society of Petroleum Engineers, San Antonio, Texas, 5–8 October 1997.

[18] A.P. Prudnikov, Y.A. Brychkov, O.I. Marichev, Integrals and Series, vol 5: Inverse Laplace Transforms, Gordon and Breach Science Publishers, 1992.

[19] M. Peyron, G.K. Pierens, A.J. Lucas, L.D. Hall, R.C. Stewart, The modified stretched-exponential model for characterization of nmr relaxation in porous media, J. Magn. Reson. Ser. A 118 (2) (1996) 214–220. <http://www.sciencedirect.com/science/article/pii/S1064185896900297>.

[20] F. Gruber, L. Venkataramanan, D. Freed, T. Habashy, A new approach for the estimation of the porosity in NMR, in: Acoustics, Speech and Signal Processing (ICASSP), 2011 IEEE International Conference on, May 2011, pp. 1797–1800.

[21] J.P. Butler, J.A. Reeds, S.V. Dawson, Estimating solutions of the first kind integral equations with nonnegative constraints and optimal smoothing, SIAM J. Numer. Anal. 18 (3) (1981) 381–397.

[22] M. Bertero, Linear inverse and ill-posed problems, in Advances in Electronics and Electron Physics, ed. P.W. Hawkes, Vol.75, 1–120, Academic Press, New York, 1989.